The Astrophysical Journal, 770:2 (9pp), 2013 June 10 doi:10.1088/0004-637X/770/1/2

MEASUREMENT OF THE ISOTOPIC COMPOSITION OF HYDROGEN AND HELIUM NUCLEI IN COSMIC RAYS WITH THE PAMELA EXPERIMENT

O. Adriani[1,2], G. C. Barbarino[3,4], G. A. Bazilevskaya[5], R. Bellotti[6,7], M. Boezio[8], E. A. Bogomolov[9], M. Bongi[1,2], V. Bonvicini[8], S. Borisov[10,11,12], S. Bottai[2], A. Bruno[6,7], F. Cafagna[7], D. Campana[4], R. Carbone[8], P. Carlson[13], M. Casolino[10,14], G. Castellini[15], I. A. Danilchenko[12], M. P. De Pascale[10,11,21], C. De Santis[11], N. De Simone[11], V. Di Felice[11], V. Formato[8,16], A. M. Galper[12], A. V. Karelin[12], S. V. Koldashov[12], S. Koldobskiy[12], S. Y. Krutkov[9], A. N. Kvashnin[5], A. Leonov[12], V. Malakhov[12], L. Marcelli[11], A. G. Mayorov[12], W. Menn[17], V. V. Mikhailov[12], E. Mocchiutti[8], A. Monaco[6,7], N. Mori[2], N. Nikonov[9,10,11], G. Osteria[4], F. Palma[10,11], P. Papini[2], M. Pearce[13], P. Picozza[10,11], C. Pizzolotto[8,18,19], M. Ricci[20], S. B. Ricciarini[15], L. Rossetto[13], R. Sarkar[8], M. Simon[17], R. Sparvoli[10,11], P. Spillantini[1,2], Y. I. Stozhkov[5], A. Vacchi[8], E. Vannuccini[2], G. Vasilyev[9], S. A. Voronov[12], Y. T. Yurkin[12], J. Wu[13,22], G. Zampa[8], N. Zampa[8], and V. G. Zverev[12]

[1] Department of Physics, University of Florence, I-50019 Sesto Fiorentino, Florence, Italy
[2] INFN, Sezione di Florence, I-50019 Sesto Fiorentino, Florence, Italy
[3] Department of Physics, University of Naples "Federico II," I-80126 Naples, Italy
[4] INFN, Sezione di Naples, I-80126 Naples, Italy
[5] Lebedev Physical Institute, RU-119991, Moscow, Russia
[6] Department of Physics, University of Bari, I-70126 Bari, Italy
[7] INFN, Sezione di Bari, I-70126 Bari, Italy
[8] INFN, Sezione di Trieste, I-34149 Trieste, Italy
[9] Ioffe Physical Technical Institute, RU-194021 St. Petersburg, Russia
[10] INFN, Sezione di Rome "Tor Vergata," I-00133 Rome, Italy
[11] Department of Physics, University of Rome "Tor Vergata," I-00133 Rome, Italy
[12] National Research Nuclear University MEPhI, RU-115409 Moscow, Russia
[13] KTH, Department of Physics, and the Oskar Klein Centre for Cosmoparticle Physics, AlbaNova University Centre, SE-10691 Stockholm, Sweden
[14] RIKEN, Advanced Science Institute, Wako-shi, Saitama, Japan
[15] IFAC, I-50019 Sesto Fiorentino, Florence, Italy
[16] Department of Physics, University of Trieste, I-34147 Trieste, Italy
[17] Department of Physics, Universität Siegen, D-57068 Siegen, Germany
[18] INFN, Sezione di Perugia, I-06123 Perugia, Italy
[19] Agenzia Spaziale Italiana (ASI) Science Data Center, I-00044 Frascati, Italy
[20] INFN, Laboratori Nazionali di Frascati, Via Enrico Fermi 40, I-00044 Frascati, Italy
Received 2012 November 21; accepted 2013 April 18; published 2013 May 16

ABSTRACT

The satellite-borne experiment PAMELA has been used to make new measurements of cosmic ray H and He isotopes. The isotopic composition was measured between 100 and 600 MeV/n for hydrogen and between 100 and 900 MeV/n for helium isotopes over the 23rd solar minimum from 2006 July to 2007 December. The energy spectrum of these components carries fundamental information regarding the propagation of cosmic rays in the galaxy which are competitive with those obtained from other secondary to primary measurements such as B/C.

Key words: astroparticle physics – cosmic rays

Online-only material: color figures

1. INTRODUCTION

Hydrogen and helium isotopes in cosmic rays are generally believed to be of secondary origin, resulting from the nuclear interactions of primary cosmic-ray protons and ^{4}He with the interstellar medium, mainly through spallation of primary ^{4}He nuclei or through the reaction $p + p \rightarrow {}^2\mathrm{H} + \pi^+$. These isotopes can be used to study and constrain parameters in propagation models for galactic cosmic rays (GCRs; Strong et al. 2007; Tomassetti 2012; Coste et al. 2012). ^{2}H and ^{3}He are the most abundant secondary isotopes in GCRs and have peculiar features: ^{2}H is the only secondary species (apart from antiprotons) that can also be produced in proton–proton interactions and ^{3}He is the only secondary fragment with a A/Z significantly different from two (A and Z being, respectively, the mass and charge number).

The importance of light isotopes has been known for about 40 yr, when the first measurements became available (Garcia-Munoz et al. 1975a, 1975b; Mewaldt et al. 1976; Leech & O' Gallagher 1978). Measurements require very good mass resolution, a challenge for instruments deployed in space. With the exception of the results from AMS-01 (Aguilar et al. 2011) most of the measurements were performed using stratospheric balloons (Wang et al. 2002; Reimer et al. 1998; Wefel et al. 1995; Webber et al. 1991; Beatty et al. 1993), where the residual atmosphere above the instrument caused a non-negligible background of secondary particles. The atmospheric background estimation is subject to large uncertainties (e.g., the limited knowledge of isotope production cross sections). Due to these limitations, experimental errors are generally very large and the focus of measurements therefore shifted to other secondary species, like boron or sub-iron nuclei (Strong & Moskalenko 1998).

The light-isotope quartet offers an independent unique way to address the issue of "universality in GCR propagation," which

[21] Deceased.
[22] On leave from School of Mathematics and Physics, China University of Geosciences, CN-430074 Wuhan, China.

can be crucial when analyzing antiproton and positron spectra to search for possible primary signals (see, e.g., Stephens 1989). The PAMELA experiment has been observing GCRs over the 23rd solar minimum since 2006 July at an altitude ranging from ~350 km to ~600 km on board of the Russian *Resurs-DK1* satellite which executes a quasi-polar orbit. The low-Earth orbit allows PAMELA to perform measurements in an environment free from the background induced by atmospheric cosmic rays.

The results presented here are based on the data set collected by PAMELA between 2006 July and 2007 December. From about 10^9 triggered events, accumulated during a total acquisition time of 528 days, 5,378,795 hydrogen nuclei were selected in the energy interval between 100 and 600 MeV/n and 1,749,964 helium nuclei between 100 and 900 MeV/n. The data presented here replace and complete the preliminary results presented in Casolino et al. (2011). A more complete evaluation of the selection efficiencies and contamination due to an improved simulation resulted in better reconstructed ^{2}H and ^{3}He spectra and ^{3}He/^{4}He ratio.

2. THE PAMELA APPARATUS

The PAMELA spectrometer was designed and built to study the antimatter component of cosmic rays from tens of MeV up to hundreds of GeV and with a significant increase in statistics with respect to previous experiments. To reach this goal the apparatus was optimized for the study of $Z = 1$ particles and to reach a high level of electron–proton discrimination.

The core of the instrument (Figure 1) is a permanent magnet with an almost uniform magnetic field inside the magnetic cavity which houses six planes of double-sided silicon microstrip detectors to measure the trajectory of incoming particles. The spatial resolution is ~3 μm in the bending view (also referred to as the x-view) and ~11 μm in the non-bending view (also referred to as the y-view). The main task of the magnetic spectrometer is to measure particle rigidity $\rho = pc/Ze$ (p and Ze being, respectively, the particle momentum and charge, and c the speed of light) and ionization energy losses (dE/dx).

The time-of-flight (ToF) system comprises three double layers of plastic scintillator paddles (S1, S2, and S3, as shown in Figure 1) with the first two placed above and the third immediately below the magnetic spectrometer. The ToF system provides 12 independent measurements of the particle velocity, $\beta = v/c$, combining the time of passage information with the track length derived from the magnetic spectrometer. By measuring the particle velocity the ToF system discriminates between particles moving downward and splash albedo particles moving upward thus enabling the spectrometer to establish the sign of the particle charge. The ToF system also provides six independent dE/dx measurements, one for each scintillator plane.

A silicon-tungsten electromagnetic sampling calorimeter made of 44 single-sided silicon microstrip detectors interleaved with 22 plates of tungsten absorber (for a total of 16.3 X_0) mounted below the spectrometer is used for hadron/lepton separation with a shower tail catcher scintillator (S4). A neutron detector at the bottom of the apparatus helps to increase this separation.

The anticoincidence (AC) system comprises four scintillators surrounding the magnet (CAS), one surrounding the cavity entrance (CAT) and four scintillators surrounding the volume between S1 and S2 (CARD). The system is used to reject events where the presence of secondary particles generates a false trigger or the primary particle suffers an inelastic interaction.

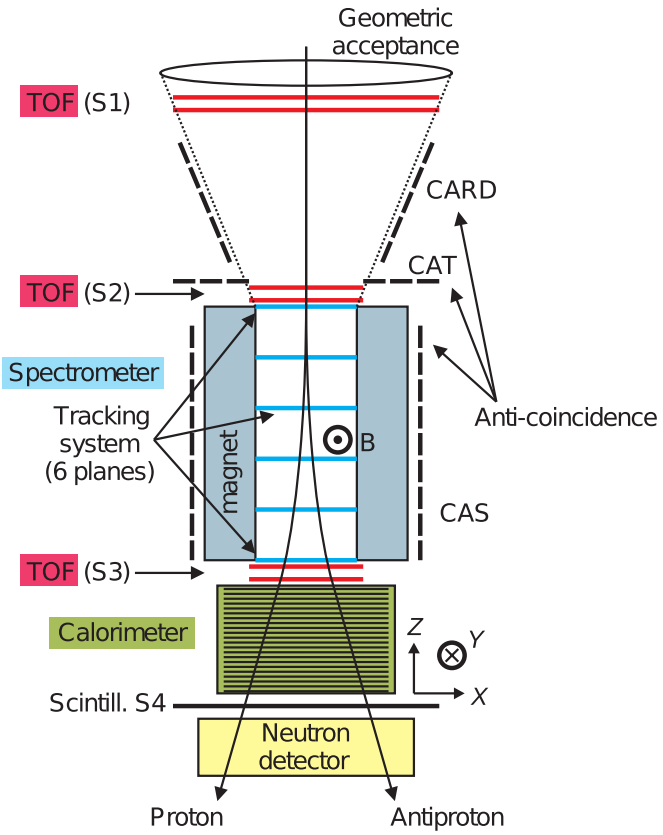

Figure 1. A schematic overview of the PAMELA satellite experiment. The experiment stands ~1.3 m high and, from top to bottom, consists of a time-of-flight (ToF) system (S1, S2, S3 scintillator planes), an anticoincidence shield system, a permanent magnet spectrometer (the magnetic field runs in the y-direction), a silicon-tungsten electromagnetic calorimeter, a shower tail scintillator (S4), and a neutron detector.

(A color version of this figure is available in the online journal.)

The readout electronics, the interfaces with the CPU, and all primary and secondary power supplies are housed around the detectors. The apparatus is enclosed in a pressurized container attached to the side of the *Resurs-DK1* satellite. The total weight of PAMELA is 470 kg while the power consumption is 355 W. A more detailed description of the instruments and the data handling can be found in Picozza et al. (2007).

3. DATA ANALYSIS

3.1. Event Selection

The month of 2006 December was discarded to avoid possible biases from the solar particle events that took place during December 13 and 14. The event selections adopted are similar to those used in previous works on the high energy proton and helium fluxes (Adriani et al. 2011) and on the time dependence of the low energy proton flux (Adriani et al. 2013).

3.1.1. Event Quality Selections

In order to ensure a reliable event reconstruction a set of basic criteria was developed. The aim of these requirements was to select positively charged particles with a precise measurement of the absolute value of the particle rigidity and velocity. Furthermore, events with more than one track, likely to be products of hadronic interactions occurring in the top part of the apparatus, were rejected.

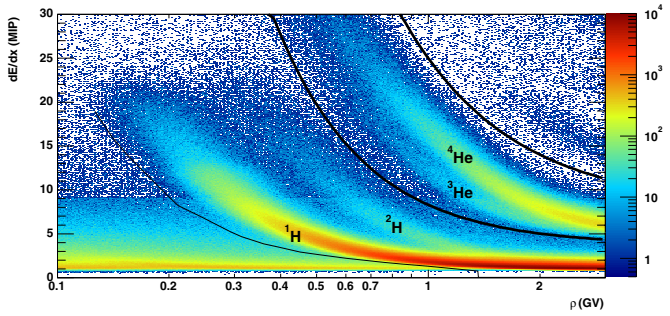

Figure 2. Energy loss in the silicon detectors of the tracking system (mean energy deposition in all planes hit) as a function of reconstructed rigidity for positively charged particles. The hydrogen and helium bands are clearly visible. The black lines represent the selection for H and He nuclei.

(A color version of this figure is available in the online journal.)

Events were selected requiring:

1. A single track fitted within the spectrometer fiducial volume where the reconstructed track is at least 1.5 mm away from the magnet walls.
2. A positive value for the reconstructed track curvature.
3. Selected tracks must have at least four hits on the x-view and at least three hits on the y-view to ensure a good rigidity reconstruction.
4. A maximum of one hit paddle in the two top planes of the ToF system.
5. The hit paddles in S1 and S2 must match the extrapolated trajectory from the spectrometer.
6. A positive value for the measured ToF. This selection ensures that the particle enters PAMELA from above.
7. For the selection of the hydrogen sample no activity in the CARD and CAT scintillators of the anticoincidence system is required.

The anticoincidence selections on the hydrogen sample were necessary since most secondary particles that entered the PAMELA fiducial acceptance were by-products of hadronic interactions taking place in the aluminum dome or in the S1 and S2 scintillators. Such particles were generally accompanied by other secondary particles which hit the anticoincidence detectors. For the selection of the helium sample there were no anticoincidence requirements since contamination by secondary helium coming from heavier nuclei spallation is negligible.

3.1.2. Galactic Particle Selection

The *Resurs-DK1* satellite orbital information was used to estimate the local geomagnetic cutoff, G, in the Störmer approximation (Shea et al. 1987) using the IGRF magnetic field model (MacMillan & Maus 2005) along the orbit. The maximum zenith angle for events entering the PAMELA acceptance was 24°with a mean value of 10°. To select the primary (galactic) cosmic ray component particles were binned by requiring that $\rho_m > k \cdot G$, where ρ_m is the lowest edge of the rigidity interval and $k = 1.3$ is a safety factor required to remove any directionality effects due to the Earth's penumbral regions. Galactic particles losing energy while crossing the detector may be rejected by this selection. This effect is accounted for using Monte Carlo simulations.

3.1.3. Charge Selection

Particle charge identification relies on the ionization measurements provided by the magnetic spectrometer. Depending on the number of hit planes there can be up to 12 dE/dx measurements. The arithmetic mean of those measurements is shown in Figure 2. A rigidity dependent selection on the mean dE/dx from the spectrometer is used to select $Z = 1$ or $Z = 2$ candidates and is depicted by the solid lines in Figure 2.

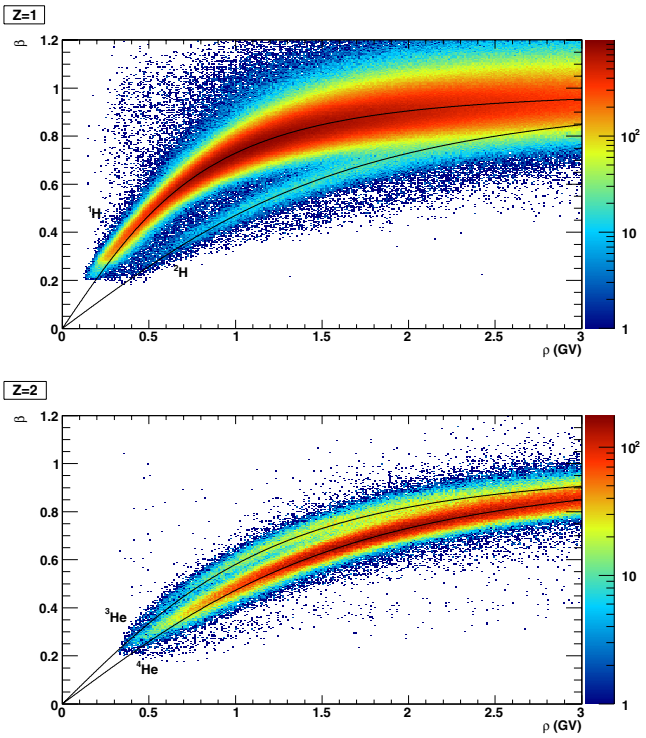

Figure 3. Mass separation for $Z = 1$ (top) and $Z = 2$ (bottom) particles using the β-rigidity method. The black lines represent the expectations for each isotope.

(A color version of this figure is available in the online journal.)

The residual contamination of $Z = 2$ particles in the $Z = 1$ sample was studied selecting helium events using the dE/dx information from the ToF system, and then applying the $Z = 1$ selection previously described. The fraction of misidentified helium events was found to be less than 10^{-4}. Since the ^{2}H/^{4}He ratio is roughly 0.15 the resulting contamination in the ^{2}H sample from misidentified ^{4}He was estimated less than 10^{-3}. Similarly, the $Z = 1$ residual contamination as well as contamination by heavier nuclei in the $Z = 2$ sample was estimated to be negligible.

3.2. Isotope Separation

The selection criteria described in the previous section provided clean samples of $Z = 1$ and $Z = 2$ particles. In each sample an isotopic separation at fixed rigidity is possible by reconstructing β, where

$$\beta = \left(1 + \frac{m^2}{Z^2\rho^2}\right)^{-1/2} \quad (1)$$

as shown in Figure 3 for events in the (β, ρ) plane.

Isotope separation as well as the determination of isotope fluxes was performed in intervals of kinetic energy per nucleon. Since the magnetic spectrometer measures the rigidity of particles, this implies different rigidity intervals according to the isotope under study. For example, Figure 4 shows the $1/\beta$ distributions used to select ^{1}H (top panel) and ^{2}H (bottom panel) in the kinetic energy interval 0.329–0.361 GeV/n corresponding

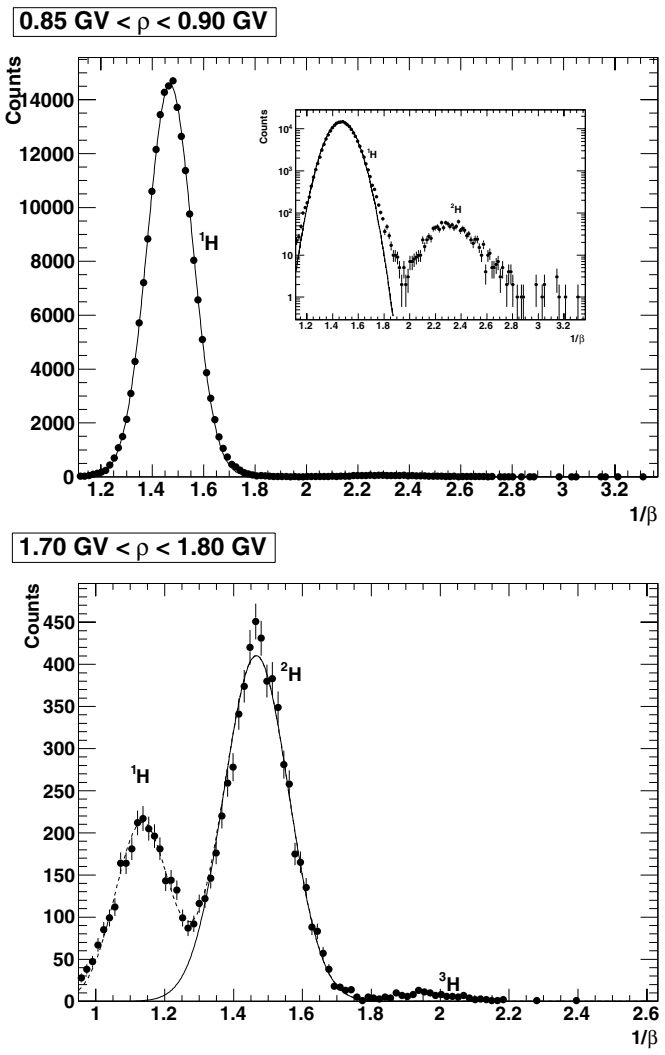

Figure 4. Examples of $1/\beta$ distributions for hydrogen in the 0.329–0.361 GeV/n kinetic energy range for ^{1}H (top) and ^{2}H (bottom). The solid line shows the estimated ^{1}H and ^{2}H signal while the dashed line shows the combined fit used in the ^{2}H case to improve the fit result. The box in the upper plot shows the same distribution with a logarithmic scale to show the ^{2}H component that is not visible on a linear scale. The ^{1}H component in the ^{2}H distribution in the bottom plot is suppressed by the additional selection shown in Figure 6. The hydrogen sample also contains a small fraction of ^{3}H events which are used to test the reliability of the Monte Carlo simulation.

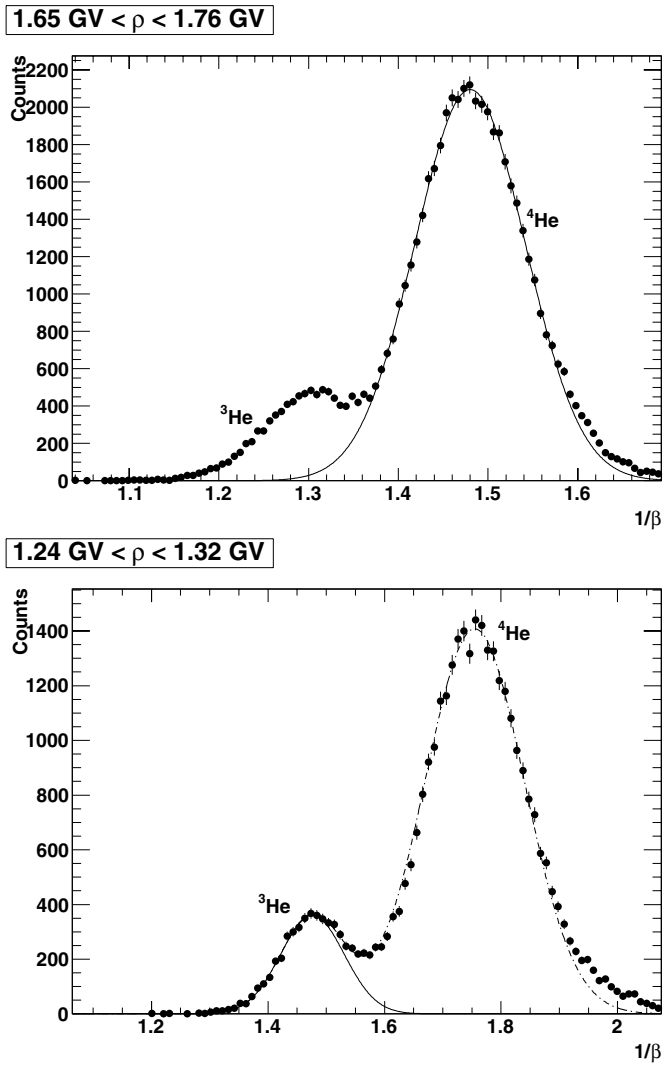

Figure 5. Examples of $1/\beta$ distributions for helium in the 0.312–0.350 GeV/n kinetic energy range for ^{4}He (top) and ^{3}He (bottom). The solid line shows the estimated ^{4}He and ^{3}He signal while the dashed line shows the combined fit used in the ^{3}He case to improve the fit result.

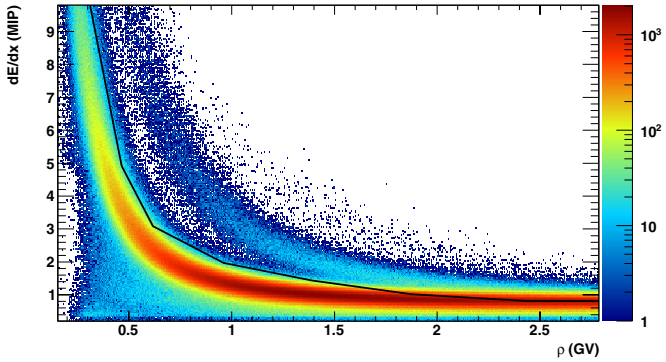

Figure 6. The lowest of the 12 energy releases in the tracking system as a function of rigidity for $Z = 1$ events. Events with energy releases above the black line were selected for the ^{2}H analysis.

(A color version of this figure is available in the online journal.)

to 0.85–0.9 GV for ^{1}H and 1.7–1.8 GV for ^{2}H. Particle counts were subsequently extracted from a Gaussian fit to the $1/\beta$ distribution in each rigidity range as shown by the solid lines in Figure 4.

Separation between ^{3}He and ^{4}He was obtained in a similar way. Figure 5 shows the $1/\beta$ distributions used to select ^{3}He (bottom panel) and ^{4}He (top panel) in the kinetic energy interval 0.312–0.350 GeV/n corresponding to 1.24–1.32 GV for ^{3}He and 1.65–1.76 GV for ^{4}He.

It should be noted that, because of the large proton background, an additional selection, based on the lowest energy release among the 12 measurements provided by the tracking system (often referred as *truncated mean*), was used to produce the $1/\beta$ distributions in the ^{2}H case. Figure 6 shows this quantity for $Z = 1$ particles. The solid line indicates the condition on the minimum energy release used for the selection.

The selected number of hydrogen and helium events are summarized in the second and third column of Tables 1 and 2.

3.3. Flux Determination

The procedure described in the previous section was used to estimate the number of ^{1}H and ^{2}H events in the $Z = 1$ sample and the number of ^{3}He and ^{4}He events in the $Z = 2$ sample.

Table 1
Number of Selected and Reconstructed Events for the $Z = 1$ Sample

Kinetic Energy Per Nucleon (GeV/n)	^{1}H Events	^{2}H Events	^{2}H Contamination	^{1}H Extrapolated Events at Top of Payload (N_{ToP})	^{2}H Extrapolated Events at Top of Payload (N_{ToP})
0.120–0.132	38927 ± 477	2179 ± 99	207 ± 9	70273 ± 867	3474 ± 187
0.132–0.144	47689 ± 521	2401 ± 60	212 ± 5	85115 ± 940	4120 ± 106
0.144–0.158	58104 ± 587	2815 ± 114	230 ± 9	102825 ± 1049	4800 ± 209
0.158–0.173	70390 ± 635	3284 ± 120	248 ± 9	122634 ± 1115	5594 ± 225
0.173–0.190	84622 ± 703	3752 ± 124	261 ± 9	145937 ± 1227	6397 ± 227
0.190–0.208	102408 ± 781	4312 ± 134	276 ± 9	177148 ± 1369	7385 ± 246
0.208–0.228	123869 ± 843	4865 ± 144	286 ± 8	212463 ± 1465	8343 ± 265
0.228–0.250	145923 ± 929	5505 ± 153	298 ± 8	248196 ± 1601	9298 ± 278
0.250–0.274	173016 ± 996	6015 ± 159	302 ± 8	291879 ± 1695	10165 ± 287
0.274–0.300	200767 ± 1105	6683 ± 173	312 ± 8	336058 ± 1868	11269 ± 310
0.300–0.329	231937 ± 1129	7419 ± 192	324 ± 8	388972 ± 1903	12635 ± 345
0.329–0.361	266950 ± 1259	8274 ± 209	339 ± 9	443768 ± 2107	14143 ± 374
0.361–0.395	303941 ± 1354	9356 ± 227	358 ± 9	506860 ± 2291	15447 ± 402
0.395–0.433	343790 ± 1389	10153 ± 245	358 ± 9	568056 ± 2315	17005 ± 432
0.433–0.475	382305 ± 1511	10922 ± 259	345 ± 8	630535 ± 2517	18588 ± 461
0.475–0.520	424071 ± 1583	11551 ± 287	310 ± 8	703994 ± 2654	20277 ± 511
0.520–0.570	466939 ± 1658	12425 ± 337	258 ± 7	775857 ± 2784	22210 ± 608

Table 2
Number of Selected and Reconstructed Events for the $Z = 2$ Sample

Kinetic Energy Per Nucleon (GeV/n)	^{4}He Events	^{3}He Events	^{4}He Extrapolated Events at Top of Payload (N_{ToP})	^{3}He Extrapolated Events at Top of Payload (N_{ToP})
0.126–0.141	21092 ± 636	1522 ± 107	32094 ± 964	2387 ± 170
0.141–0.158	24709 ± 652	1929 ± 107	37995 ± 1015	3023 ± 170
0.158–0.177	29506 ± 695	2403 ± 131	45235 ± 1068	3768 ± 208
0.177–0.198	35215 ± 817	2952 ± 143	54237 ± 1243	4645 ± 226
0.198–0.222	41078 ± 897	3583 ± 162	64104 ± 1405	5618 ± 256
0.222–0.249	47654 ± 980	4306 ± 163	74926 ± 1545	6864 ± 264
0.249–0.279	53935 ± 1077	5124 ± 183	84403 ± 1640	8203 ± 295
0.279–0.312	61541 ± 1148	6040 ± 196	98143 ± 1851	9853 ± 325
0.312–0.350	68608 ± 1145	7046 ± 207	109058 ± 1837	11645 ± 345
0.350–0.392	76090 ± 1224	8125 ± 226	121874 ± 1971	13737 ± 388
0.392–0.439	83651 ± 1268	9246 ± 255	135138 ± 2058	16080 ± 453
0.439–0.492	90552 ± 1262	10353 ± 266	143775 ± 2017	18371 ± 471
0.492–0.551	99140 ± 1422	11366 ± 286	159728 ± 2310	20577 ± 521
0.551–0.618	104636 ± 1483	12173 ± 321	167348 ± 2397	23111 ± 612
0.618–0.692	110854 ± 1665	13209 ± 332	181468 ± 2771	26133 ± 662
0.692–0.776	114097 ± 1624	13946 ± 363	186092 ± 2665	28768 ± 762
0.776–0.870	117080 ± 1768	13985 ± 362	193787 ± 2935	30778 ± 811

To derive each isotope flux the number of selected events had to be corrected for the selections efficiencies, particle losses, contamination, and energy losses. These corrections were obtained using a Monte Carlo simulation of the PAMELA apparatus based on the GEANT4 code (Agostinelli et al. 2003) and from the flight data. The simulation contains an accurate representation of the geometry and performance of the PAMELA detectors. The measured noise of each silicon plane of the spectrometer and its performance variations over the duration of the measurement were accounted for. The simulation code was validated by comparing the distributions of several significant variables with those obtained from real data. Hadronic interactions for all the isotopes under study were handled via the QGSP_BIC_HP physics list.

The following corrections to the number of selected events were applied:

1. *Selection efficiencies.* The redundant information provided by PAMELA allowed most of the selection efficiencies to be estimated directly from flight data. For example, the efficiency of the charge selections was evaluated on a sample of events selected with the ToF dE/dx measurements in the same way as described in Section 3.1.3 for the charge misidentification study. The efficiency of the tracking system was, however, obtained from the Monte Carlo simulation. The decrease in efficiency from 2006 to 2007 is due to the failure of some of the front-end chips in the tracking system. This situation was included in the Monte Carlo simulation, as discussed in Adriani et al. (2013). The efficiencies of the various selections are reported in Table 3.
2. *Hadronic interactions.* Helium and hydrogen nuclei may be lost due to hadronic interactions in the 2 mm thick aluminum pressurized container and the top scintillator detectors. The correction to the flux due to this effect was included in the PAMELA geometrical factor as follows:

$$G(E) = [1 - b(E)]\, G_F \quad (2)$$

where $G(E)$ is the effective geometrical factor used for the flux determination, $b(E)$ is a correction factor which accounts for the effect of inelastic scattering, G_F is the nominal geometrical factor which is almost constant above 1 GV

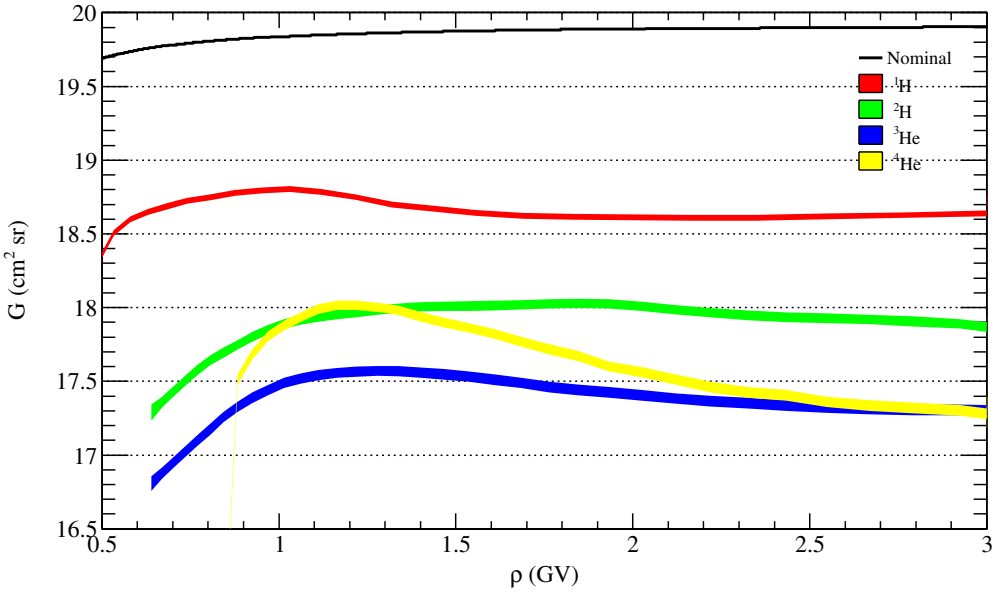

Figure 7. The nominal geometrical factor G_F as a function of rigidity (solid line). The filled bands represent the effective geometrical factor $G(E)$ for each isotope with the associated uncertainty.

(A color version of this figure is available in the online journal.)

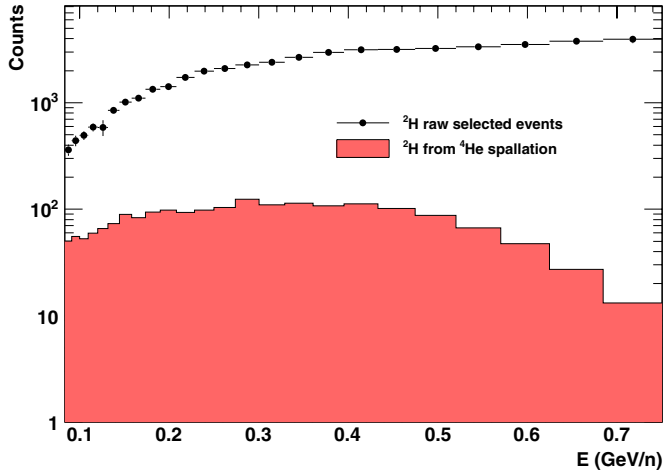

Figure 8. Raw counts for ^{2}H collected by PAMELA in 2006 together with the expected contamination from ^{4}He spallation in the top part of the apparatus.

(A color version of this figure is available in the online journal.)

and slowly decreases by ∼2% to lower energies, where the particle trajectory in the magnetic field is no longer straight. The requirement on the fiducial volume corresponds to a geometrical factor $G_F = 19.9$ cm^2 sr above 1 GV. The correction factor $b(E)$ is different for each isotope and has been derived from the Monte Carlo simulation, being ≃6% for protons, ≃10% for deuterium, and ≃13% for both helium isotopes. The nominal geometrical factor and the effective geometrical factor for each isotope are shown in Figure 7.

3. *Contamination.* The contribution to ^{2}H from ^{4}He inelastic scattering was evaluated from the simulation (Figure 8) and subtracted from the raw ^{2}H counts (see Column 4 of Table 1). The contamination in the ^{3}He sample from ^{4}He fragmentation was also evaluated and it was estimated to be less than 1%. This was included in the systematic uncertainty of the measurement.
4. *Energy loss and resolution.* The finite resolution of the magnetic spectrometer and particle slowdown due to ionization energy losses results in a distortion of the particle spectra. A Bayesian unfolding procedure, described in D'Agostini (1995), was used to derive the number of events at the top of the payload (see Adriani et al. 2011).

The flux was then calculated as follows:

$$\Phi_{\rm ToP}(E) = \frac{N_{\rm ToP}(E)}{TG(E)\Delta E} \quad (3)$$

where $N_{\rm ToP}(E)$ is the unfolded particle count for energy E, also corrected for all the selection efficiencies (see Tables 1 and 2, rightmost two columns), ΔE is the energy bin width, and $G(E)$ is the effective geometrical factor. The live time, T, as evaluated by the trigger system, depends on the orbital selection as described in Section 3.1.2 (e.g., see Bruno 2008). The live and dead time are cross-checked with the total acquisition time measured by the on-board CPU to remove possible systematic effects in the time counting.

3.4. Systematic Uncertainties

The possible sources of systematic uncertainties considered in this analysis are listed below and are also included in Tables 4 and 5 and in Figures 9–11.

1. *Quality of the $1/\beta$ fit.* The quality of the Gaussian fit procedure was tested using the truncated mean of the energy deposited in the electromagnetic calorimeter to select pure samples of ^{1}H and ^{2}H from non-interacting events. The two samples were then merged to form a control sample for the fitting algorithm. The number of reconstructed events from the Gaussian fit was found to agree with the number of events selected with the calorimeter, so no systematic uncertainty was assigned to this procedure.
2. *Selection efficiencies.* The estimation of the selection efficiencies is affected by a statistical error due to the finite size of the sample used for the efficiency evaluation. This error was considered and propagated as a systematic uncertainty. For the efficiency of the ToF and AC selections this uncertainty is 0.21% at low energy (120 MeV/n)

Table 3
Selection Efficiencies, Divided by Detector

	^{1}H	^{2}H	^{3}He	^{4}He
ToF and AC selections	$88.99\% \pm 0.13\%$	$88.51\% \pm 0.18\%$	$89.0\% \pm 0.4\%$	$88.1\% \pm 0.4\%$
Tracker selections (2006)	$88.6\% \pm 0.2\%$	$87.1\% \pm 0.3\%$	$89.5\% \pm 0.4\%$	$88.3\% \pm 0.4\%$
Tracker selections (2007)	$62.2\% \pm 0.3\%$	$60.8\% \pm 0.4\%$	$61.2\% \pm 0.6\%$	$62.1\% \pm 0.7\%$
Tracker dE/dx selection	100%	$96.67\% \pm 0.13\%$	$95.5\% \pm 0.2\%$	100%
Total efficiency (2006)	$78.8\% \pm 0.3\%$	$74.5\% \pm 0.5\%$	$76.1\% \pm 0.8\%$	$77.8\% \pm 0.7\%$
Total efficiency (2007)	$55.4\% \pm 0.5\%$	$52.0\% \pm 0.5\%$	$52.0\% \pm 0.9\%$	$54.7\% \pm 1.2\%$

Table 4
Hydrogen Isotope Fluxes and Their Ratio

Kinetic Energy at Top of Payload (GeV n^{-1})	^{1}H Flux (GeV n^{-1} m^2 s sr)$^{-1}$	^{2}H Flux (GeV n^{-1} m^2 s sr)$^{-1}$	^{2}H/^{1}H
0.120–0.132	$(9.86 \pm 0.15 \pm 0.31) \times 10^2$	$(30.8 \pm 1.8 \pm 1.0)$	$(3.12 \pm 0.19 \pm 0.20) \times 10^{-2}$
0.132–0.144	$(1.064 \pm 0.014 \pm 0.030) \times 10^3$	$(33.0 \pm 1.6 \pm 0.9)$	$(3.10 \pm 0.15 \pm 0.18) \times 10^{-2}$
0.144–0.158	$(1.136 \pm 0.013 \pm 0.029) \times 10^3$	$(34.2 \pm 1.4 \pm 0.9)$	$(3.01 \pm 0.13 \pm 0.16) \times 10^{-2}$
0.158–0.173	$(1.182 \pm 0.012 \pm 0.028) \times 10^3$	$(35.1 \pm 1.4 \pm 0.8)$	$(2.97 \pm 0.12 \pm 0.14) \times 10^{-2}$
0.173–0.190	$(1.233 \pm 0.012 \pm 0.027) \times 10^3$	$(35.3 \pm 1.3 \pm 0.8)$	$(2.86 \pm 0.11 \pm 0.13) \times 10^{-2}$
0.190–0.208	$(1.300 \pm 0.011 \pm 0.027) \times 10^3$	$(36.6 \pm 1.3 \pm 0.8)$	$(2.81 \pm 0.10 \pm 0.12) \times 10^{-2}$
0.208–0.228	$(1.351 \pm 0.010 \pm 0.027) \times 10^3$	$(37.1 \pm 1.2 \pm 0.7)$	$(2.74 \pm 0.09 \pm 0.11) \times 10^{-2}$
0.228–0.250	$(1.405 \pm 0.010 \pm 0.027) \times 10^3$	$(36.3 \pm 1.1 \pm 0.7)$	$(2.58 \pm 0.08 \pm 0.10) \times 10^{-2}$
0.250–0.274	$(1.453 \pm 0.009 \pm 0.027) \times 10^3$	$(34.5 \pm 1.0 \pm 0.6)$	$(2.37 \pm 0.07 \pm 0.09) \times 10^{-2}$
0.274–0.300	$(1.486 \pm 0.008 \pm 0.027) \times 10^3$	$(33.9 \pm 0.9 \pm 0.6)$	$(2.28 \pm 0.06 \pm 0.08) \times 10^{-2}$
0.300–0.329	$(1.514 \pm 0.008 \pm 0.027) \times 10^3$	$(34.1 \pm 0.9 \pm 0.6)$	$(2.25 \pm 0.06 \pm 0.08) \times 10^{-2}$
0.329–0.361	$(1.517 \pm 0.007 \pm 0.026) \times 10^3$	$(33.6 \pm 0.9 \pm 0.6)$	$(2.22 \pm 0.06 \pm 0.08) \times 10^{-2}$
0.361–0.395	$(1.520 \pm 0.007 \pm 0.026) \times 10^3$	$(32.0 \pm 0.8 \pm 0.6)$	$(2.10 \pm 0.06 \pm 0.07) \times 10^{-2}$
0.395–0.433	$(1.484 \pm 0.006 \pm 0.025) \times 10^3$	$(31.4 \pm 0.8 \pm 0.6)$	$(2.11 \pm 0.05 \pm 0.07) \times 10^{-2}$
0.433–0.475	$(1.480 \pm 0.006 \pm 0.025) \times 10^3$	$(30.6 \pm 0.8 \pm 0.5)$	$(2.07 \pm 0.05 \pm 0.07) \times 10^{-2}$
0.475–0.520	$(1.499 \pm 0.006 \pm 0.025) \times 10^3$	$(29.9 \pm 0.8 \pm 0.5)$	$(2.00 \pm 0.05 \pm 0.07) \times 10^{-2}$
0.520–0.570	$(1.429 \pm 0.005 \pm 0.024) \times 10^3$	$(29.0 \pm 0.8 \pm 0.5)$	$(2.03 \pm 0.06 \pm 0.07) \times 10^{-2}$

Note. Errors are statistical and systematics, respectively.

Table 5
Helium Isotope Fluxes and Their Ratio

Kinetic Energy at Top of Payload (GeV n^{-1})	^{4}He Flux (GeV n^{-1} m^2 s sr)$^{-1}$	^{3}He Flux (GeV n^{-1} m^2 s sr)$^{-1}$	^{3}He/^{4}He
0.126–0.141	$(2.03 \pm 0.06 \pm 0.04) \times 10^2$	$(17.1 \pm 1.8 \pm 0.4)$	$(8.4 \pm 0.9 \pm 0.4) \times 10^{-2}$
0.141–0.158	$(2.20 \pm 0.06 \pm 0.04) \times 10^2$	$(21.3 \pm 1.7 \pm 0.5)$	$(9.7 \pm 0.8 \pm 0.4) \times 10^{-2}$
0.158–0.177	$(2.27 \pm 0.06 \pm 0.04) \times 10^2$	$(23.4 \pm 1.5 \pm 0.5)$	$(1.03 \pm 0.07 \pm 0.04) \times 10^{-1}$
0.177–0.198	$(2.33 \pm 0.06 \pm 0.04) \times 10^2$	$(24.8 \pm 1.4 \pm 0.5)$	$(1.06 \pm 0.06 \pm 0.04) \times 10^{-1}$
0.198–0.222	$(2.38 \pm 0.05 \pm 0.04) \times 10^2$	$(25.4 \pm 1.2 \pm 0.5)$	$(1.07 \pm 0.06 \pm 0.04) \times 10^{-1}$
0.222–0.249	$(2.42 \pm 0.05 \pm 0.04) \times 10^2$	$(26.7 \pm 1.2 \pm 0.5)$	$(1.10 \pm 0.05 \pm 0.04) \times 10^{-1}$
0.249–0.279	$(2.39 \pm 0.05 \pm 0.04) \times 10^2$	$(27.3 \pm 1.0 \pm 0.5)$	$(1.14 \pm 0.05 \pm 0.04) \times 10^{-1}$
0.279–0.312	$(2.37 \pm 0.04 \pm 0.04) \times 10^2$	$(28.2 \pm 1.0 \pm 0.5)$	$(1.19 \pm 0.05 \pm 0.04) \times 10^{-1}$
0.312–0.350	$(2.29 \pm 0.04 \pm 0.04) \times 10^2$	$(28.4 \pm 0.9 \pm 0.5)$	$(1.24 \pm 0.04 \pm 0.04) \times 10^{-1}$
0.350–0.392	$(2.22 \pm 0.04 \pm 0.04) \times 10^2$	$(28.9 \pm 0.8 \pm 0.6)$	$(1.30 \pm 0.04 \pm 0.05) \times 10^{-1}$
0.392–0.439	$(2.11 \pm 0.03 \pm 0.04) \times 10^2$	$(29.2 \pm 0.8 \pm 0.6)$	$(1.39 \pm 0.04 \pm 0.05) \times 10^{-1}$
0.439–0.492	$(1.93 \pm 0.03 \pm 0.03) \times 10^2$	$(28.6 \pm 0.8 \pm 0.6)$	$(1.49 \pm 0.04 \pm 0.06) \times 10^{-1}$
0.492–0.551	$(1.84 \pm 0.03 \pm 0.03) \times 10^2$	$(27.3 \pm 0.7 \pm 0.6)$	$(1.49 \pm 0.04 \pm 0.06) \times 10^{-1}$
0.551–0.618	$(1.72 \pm 0.02 \pm 0.03) \times 10^2$	$(26.5 \pm 0.7 \pm 0.5)$	$(1.55 \pm 0.05 \pm 0.06) \times 10^{-1}$
0.618–0.692	$(1.59 \pm 0.02 \pm 0.03) \times 10^2$	$(25.4 \pm 0.7 \pm 0.6)$	$(1.60 \pm 0.05 \pm 0.06) \times 10^{-1}$
0.692–0.776	$(1.44 \pm 0.02 \pm 0.03) \times 10^2$	$(24.5 \pm 0.6 \pm 0.5)$	$(1.70 \pm 0.05 \pm 0.07) \times 10^{-1}$
0.776–0.870	$(1.292 \pm 0.020 \pm 0.023) \times 10^2$	$(23.0 \pm 0.6 \pm 0.5)$	$(1.78 \pm 0.05 \pm 0.07) \times 10^{-1}$

Note. Errors are statistical and systematics, respectively.

and drops to 0.14% at high energy (600–900 MeV/n). For the tracker selections the uncertainty is 0.3% at low energy increasing to 0.4% at high energy.

3. *Galactic particle selection.* The correction for particles lost due to this selection has an uncertainty, due to the size of the Monte Carlo sample, which decreases from 6% to 0.07% as the energy increases from 120 MeV/n to 900 MeV/n.
4. *Contamination subtraction.* The subtraction of the contamination results in a systematic uncertainty on the ^{2}H flux of 1.9% at low energy dropping below 0.1% at 300 MeV/n

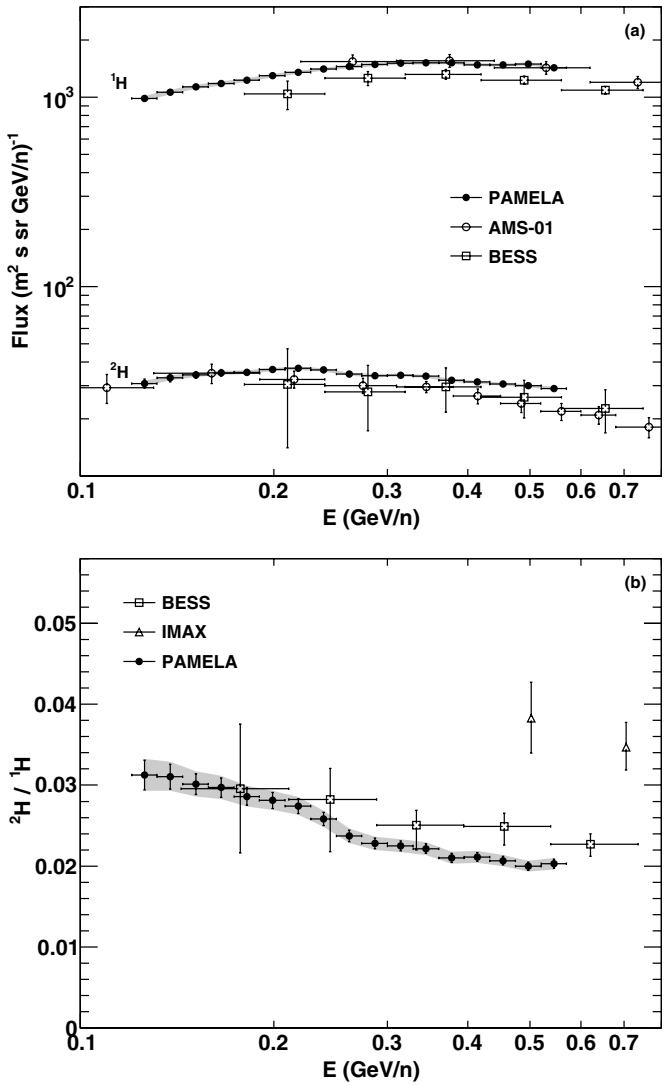

Figure 9. ^{1}H and ^{2}H absolute fluxes (a) and their ratio (b) compared to previous experiments: AMS-01 (Aguilar et al. 2002, 2011), BESS (Wang et al. 2002), and IMAX (Reimer et al. 1998). The error bars show the statistical uncertainty while shaded areas show the systematic uncertainty.

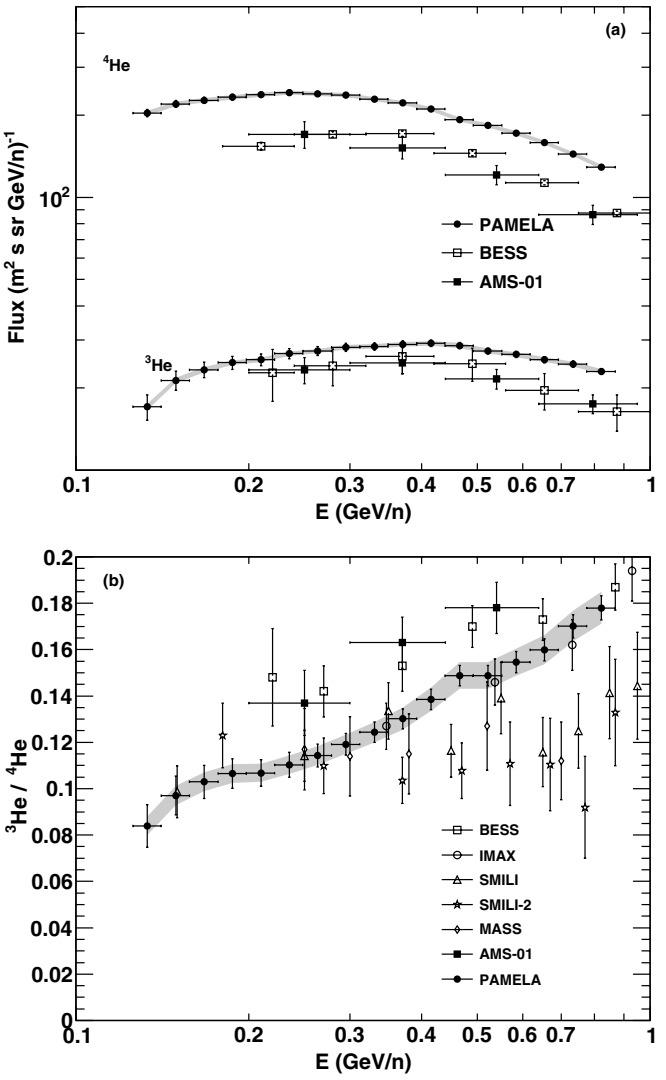

Figure 10. ^{4}He and ^{3}He absolute fluxes (a) and their ratio (b) compared to previous experiments: AMS (Aguilar et al. 2011), BESS (Wang et al. 2002), IMAX (Reimer et al. 1998), SMILI-2(Wefel et al. 1995), MASS (Webber et al. 1991), and SMILI-1 (Beatty et al. 1993). The error bars show statistical uncertainty while shaded areas show systematic uncertainty.

due to the finite size of the Monte Carlo sample. To test the validity of the Monte Carlo simulation the ^{3}H component, identified as the additional cluster of events at low β in the hydrogen sample visible in Figure 4, was used. The ^{3}H events are created by ^{4}He spallation in the top part of the apparatus since no tritium of galactic origin should survive propagation to Earth. The observed number of ^{3}H events was used to test that the Monte Carlo simulation correctly inferred the number of ^{2}H events coming from ^{4}He fragmentation. For example, for the 2006 data set in the rigidity range between 1.7 GV and 1.8 GV the flight data sample contains 136 ± 17 tritium events, while 110 ± 15 events are expected according to the Monte Carlo simulation (Figure 4). Simulation and flight data were in agreement within a 10% tolerance. This discrepancy was treated as an additional systematic uncertainty on the estimated number of contamination events. The 10% systematic uncertainty on the ^{2}H contamination translates in an additional 1% uncertainty on the number of reconstructed ^{2}H events.

5. *Geometrical factor.* The uncertainty on the effective geometrical factor as estimated from the Monte Carlo simulation is almost independent of energy and amounts to 0.18%.
6. *Unfolding procedure.* As discussed in Adriani et al. (2011), two possible systematic effects have been studied regarding the unfolding procedure: the uncertainty associated with the simulated smearing matrix and the intrinsic accuracy of the procedure. The former was constrained by checking for compatibility between measured and simulated spatial residuals and found it to be negligible. The latter was estimated by folding and unfolding a known spectral shape with the spectrometer response and was found to be 2%, independent of energy.

4. RESULTS

Figures 9 and 10 show hydrogen and helium isotope fluxes (top) and the ratios of the fluxes (bottom). The results are also reported in Tables 4 and 5. Figure 11 shows the ^{2}H/^{4}He ratio as a function of kinetic energy per nucleon, compared to previous measurements (Aguilar et al. 2011; Wang et al. 2002; Reimer et al. 1998; Wefel et al. 1995; Webber et al. 1991; Beatty

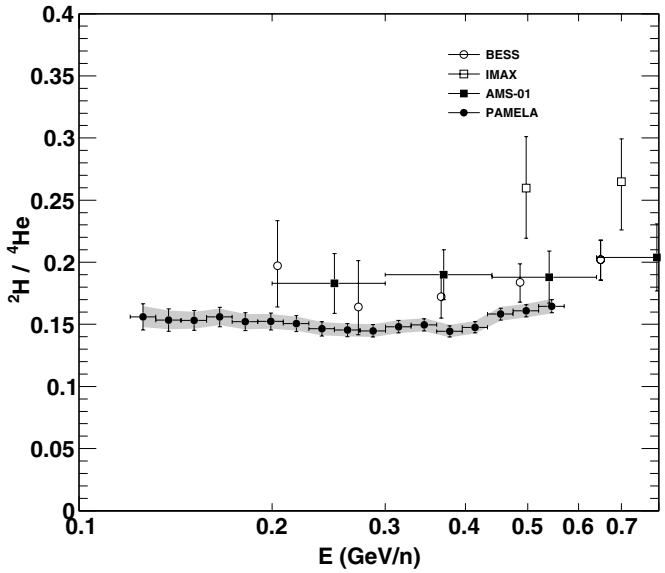

Figure 11. ^{2}H/^{4}He ratio compared to previous experiments: AMS-01 (Aguilar et al. 2011), BESS (Wang et al. 2002), and IMAX (Reimer et al. 1998). The error bars show statistical uncertainty while shaded areas show systematic uncertainty.

et al. 1993). It is worth noting that flux ratios (in particular the ^{3}He/^{4}He ratio), if modulated using the force-field approximation (Gleeson & Axford 1968), show very little dependence on solar activity and can therefore be used to discriminate between various propagation models of GCR in the Galaxy.

The PAMELA results are the most precise to date. Considering the relatively large spread in the existing data, PAMELA results agree with previous measurements, in particular with BESS results for ^{2}H and IMAX results for ^{3}He. Previous measurements are affected by large uncertainties and, for ^{3}He where more measurements are available, there is a large spread between data. All the measurements displayed in Figures 9–11, except AMS-01, are from balloon-borne experiments and are affected by a non-negligible background of atmospheric secondary particles.

A high precision measurement of the H and He isotope quartet abundances represents a significant step forward in modeling the origin and propagation of GCRs. The constraints on diffusion-model parameters set by the quartet (^{1}H, ^{2}H, ^{3}He, and ^{4}He) were recently revisited (Coste et al. 2012). It was found that the constraints on the parameters were competitive with those obtained from the B/C flux ratio analysis and available data supported the universality of GCR propagation in the Galaxy. The tightest constraint was obtained when the He flux was included in the fit. This is because at energies of a few GeV about 10% of He is from fragmentation of heavier nuclei, which is a non-negligible amount given the precision (1% statistical) of the PAMELA He data (Adriani et al. 2011).

REFERENCES

Adriani, O., Barbarino, G. C., Bazilevskaya, G. A., et al. 2011, Sci, 332, 69
Adriani, O., Barbarino, G. C., Bazilevskaya, G. A., et al. 2013, ApJ, 765, 91
Agostinelli, S., Allison, J., Amako, K., et al. 2003, NIMPA, 506, 250
AMS Collaboration, Aguilar, M., Alcaraz, J., et al. 2002, PhR, 366, 331
Aguilar, M., Alcaraz, J., Allaby, J., et al. 2011, ApJ, 736, 105
Beatty, J. J., Ficenec, D. J., Tobias, S., et al. 1993, ApJ, 413, 268
Bruno, A. 2008, PhD thesis, University of Bari
Casolino, M., de Santis, C., de Simone, N., et al. 2011, ASTRA, 7, 465
Coste, B., Derome, L., Maurin, D., & Putze, A. 2012, A&A, 539, A88
D'Agostini, G. 1995, NIMPA, 362, 487
Garcia-Munoz, M., Mason, G. M., & Simpson, J. A. 1975a, in the 14th International Cosmic Ray Conference, Vol. 1, 319
Garcia-Munoz, M., Mason, G. M., & Simpson, J. A. 1975b, ApJ, 202, 265
Gleeson, L. J., & Axford, W. I. 1968, ApJ, 154, 1011
Leech, H. W., & O' Gallagher, J. J. 1978, ApJ, 221, 1110
MacMillan, S., & Maus, S. 2005, EP&S, 57, 1135
Mewaldt, R. A., Stone, E. C., & Vogt, R. E. 1976, ApJ, 206, 616
Picozza, P., Galper, A. M., Castellini, G., et al. 2007, APh, 27, 296
Reimer, O., Menn, W., Hof, M., et al. 1998, ApJ, 496, 490
Shea, M. A., Smart, D. F., & Gentile, L. C. 1987, PEPI, 48, 200
Stephens, S. A. 1989, AdSpR, 9, 145
Strong, A. W., & Moskalenko, I. V. 1998, ApJ, 509, 212
Strong, A. W., Moskalenko, I. V., & Ptuskin, V. S. 2007, ARNPS, 57, 285
Tomassetti, N. 2012, Ap&SS, 342, 131
Wang, J. Z., Seo, E. S., Anraku, K., et al. 2002, ApJ, 564, 244
Webber, W. R., Golden, R. L., Stochaj, S. J., Ormes, J. F., & Strittmatter, R. E. 1991, ApJ, 380, 230
Wefel, J. P., Ahlen, S. P., Beatty, J. J., et al. 1995, in the 24th International Cosmic Ray Conference, Vol. 2, ed. N. Iucci & E. Lamanna, 630